Soft Matter

PAPER

View Article Online
View Journal | View Issue

Cite this: *Soft Matter*, 2017, **13**, 4773

Colloidal diffusion over a quenched two-dimensional random potential

Yun Su,[a] Xiao-guang Ma,[a] Pik-Yin Lai*[b] and Penger Tong *[a]

Received 27th May 2017,
Accepted 4th June 2017

DOI: 10.1039/c7sm01056g

rsc.li/soft-matter-journal

A two-layer colloidal system is developed for the study of diffusion over a quenched two-dimensional random potential. A mixture of bidisperse silica spheres is used to form a randomly packed colloidal monolayer on the bottom substrate. The corrugated surface of the bottom colloidal monolayer provides a gravitational potential field for the dilute diffusing particles in the top layer. The population probability histogram $P(x,y)$ of the diffusing particles is obtained to fully characterize the random potential landscape $U(x,y)$ *via* the Boltzmann distribution. The dynamical properties of the top diffusing particles, such as their mean square displacement (MSD), histogram of the escape time, and long-time self-diffusion coefficient, are simultaneously measured from the particle trajectories. A quantitative relationship between the long-time diffusion coefficient and the random potential is obtained, which is in good agreement with the theoretical prediction. The measured MSD reveals a wide region of subdiffusion resulting from the structural disorders. The crossover from subdiffusion to normal diffusion is explained by the Lorentz model for tracer diffusion through a heterogeneous space filled with a set of randomly distributed obstacles.

I. Introduction

Diffusion in disordered media is a common problem encountered in many practical applications.[1–3] Examples include diffusion of lithium ions through the electrodes in lithium ion batteries,[4] transport of molecules through porous media,[5,6] and anomalous relaxation in spin glasses and in macromolecules. It is also relevant to many biological applications[7,8] ranging from the dynamics of molecular motors moving along heterogeneous substrates[9] to the motion of proteins inside the cells[10–12] and on cell membranes.[13,14] There have been considerable theoretical efforts aimed at solving the problem with various models being proposed, such as the random barrier model,[15–18] the random trap model,[19–21] and the continuous random walk model.[22–24]

In contrast to the large number of theoretical and numerical studies, systematic experimental investigations aimed at testing the theoretical predictions are quite limited. This is partially due to the fact that it is quite difficult to find a well-characterized system in which one can obtain both the energetic and dynamic data simultaneously. In fact, the random potential involved to describe the actual disordered media may have different complex forms and does not always follow simple idealized forms. In particular, the analytical results currently available for diffusion in disordered media is often limited to one-dimensional (1D), and the actual random fields encountered in the experiment are often 2D and even 3D.

This situation is changed recently with the advancement of new technologies in manipulating and tracking individual colloidal particles. For example, Evstigneev *et al.*[25] used ten rotating optical tweezers on a circle to generate a 1D tilted periodic potential for the study of colloidal diffusion. Hanes *et al.*[26] used a laser beam to generate a 1D random intensity field and used it to study the diffusion dynamics of colloidal particles in the 1D random field. More recently, laser speckle patterns were used to generate a 2D random field.[27,28] In a different experiment,[29] Ma *et al.* developed a two-layer colloidal system and used it to study the diffusive barrier-crossing dynamics over a periodic potential. The periodic potential is provided by the bottom layer of colloidal spheres forming a crystalline pattern on a glass substrate. The corrugated surface of the colloidal crystal provides a 2D gravitational potential $U(x,y)$ for the diffusing particles on the top layer. Compared to the laser-generated random field, the colloidal landscape has an advantage that it is a pure potential field and does not have any non-conservative component, as the laser beam does.[30,31]

In this paper, we report a systematic experimental study of colloidal diffusion over a 2D quenched disordered potential. In the experiment, a mixture of bidisperse silica spheres is used to form a randomly packed colloidal monolayer on the bottom substrate, which provides a disordered gravitational potential field $U(x,y)$ to the diffusing particles on the top layer. With the techniques of optical microscopy and multiparticle tracking,

[a] *Department of Physics, Hong Kong University of Science and Technology, Clear Water Bay, Kowloon, Hong Kong. E-mail: penger@ust.hk*
[b] *Department of Physics and Center for Complex Systems, National Central University, Chungli District, Tao-Yuan City, Taiwan 320, Republic of China. E-mail: pylai@phy.ncu.edu.tw*

we measure the population statistics of the top layer diffusing particles and construct the potential $U(x,y)$ *via* the Boltzmann distribution. Using the simultaneously obtained energetics and dynamics information, we test the theory and demonstrate the applications of the newly constructed 2D random potential.

The remainder of the paper is organized as follows. We first introduce the theory about diffusion over periodic and random potentials in Section II. The experimental procedures and data processing methods are described in Section III. The experimental results and discussion are given in Section IV. Finally, we summarize the work in Section V.

II. Theory

A. Colloidal diffusion over a periodic potential

The motion of a Brownian particle over an external 2D potential $U(\mathbf{r})$ can be described by the mean square displacement (MSD) $\langle \Delta\mathbf{r}^2(\tau)\rangle$ as a function of delay time τ, where $\Delta\mathbf{r} = \mathbf{r}(t+\tau) - \mathbf{r}(t)$ with $\mathbf{r}(t)$ being the particle position at time t. For some periodic or random potentials $U(\mathbf{r})$, the motion of the particle was found to be diffusive at long delay time τ.[26,27,29,32] In this case, one has

$$\langle \Delta\mathbf{r}^2(\tau)\rangle = 4D_{\mathrm{L}}\tau, \tag{1}$$

where D_{L} is the long-time diffusion coefficient of the particle. For a 1D periodic potential $U(x+\lambda) = U(x)$ of period λ, Lifson and Jackson[21] obtained an analytical expression of D_{L} using the mean-first-passage-time (MFPT) approach,

$$D_{\mathrm{L}} = \frac{D_0}{R_\lambda}, \tag{2}$$

where

$$R_\lambda = \langle e^{U(x)/k_{\mathrm{B}}T}\rangle_\lambda \langle e^{-U(x)/k_{\mathrm{B}}T}\rangle_\lambda, \tag{3}$$

and $\langle\cdots\rangle_\lambda$ denotes a spatial average over the period λ. In eqn (2), $D_0 = k_{\mathrm{B}}T/\xi$ is the particle's free diffusion coefficient without the influence of $U(x)$, $k_{\mathrm{B}}T$ is the thermal energy of the particle and ξ is its friction coefficient. The MFPT for a particle to travel from the origin $x = 0$ to $x = \lambda$ is given by[34]

$$\bar{t}_1 = \frac{\lambda^2}{D_0}R_\lambda. \tag{4}$$

Eqn (2) can be extended to diffusion on a 2D lattice. In this case, the particle trajectories consist of multiple steps of transitions between the nearest neighbor sites through a quasi-1D path X, and thus one has[1,29]

$$D_{\mathrm{L}} = \frac{z}{4}\frac{D_0}{R_\lambda}, \tag{5}$$

where z is the number of the nearest neighbour sites of the 2D lattice.

The calculation of R_λ requires full knowledge of the potential $U(x)$, which is often difficult to obtain in many practical applications. When the energy barrier E_{b} associated with $U(x)$ is much larger than $k_{\mathrm{B}}T$, one may use the steepest-descent approximation to calculate R_λ and the final result is[34]

$$R_\lambda \simeq \frac{1}{\nu_1}e^{E_{\mathrm{b}}/k_{\mathrm{B}}T}, \tag{6}$$

where

$$\nu_1 = \frac{\left|U''_{\min}U''_{\max}\right|^{1/2}\lambda^2}{2\pi k_{\mathrm{B}}T}, \tag{7}$$

is the Arrhenius pre-factor. Eqn (6), which is called the Arrhenius–Kramers equation,[35,36] is known to be accurate only when $E_{\mathrm{b}}/k_{\mathrm{B}}T \gtrsim 6$–$7$.[29,37,38]

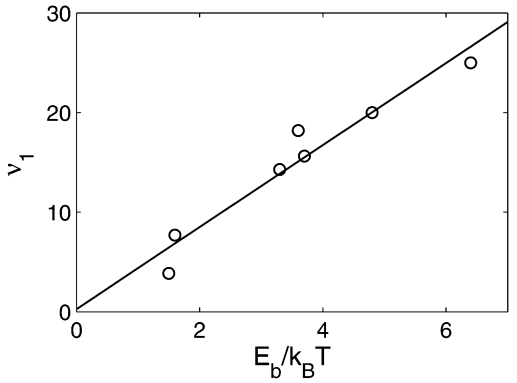

Fig. 1 Measured Arrhenius pre-factor ν_1 as a function of barrier height $E_{\mathrm{b}}/k_{\mathrm{B}}T$ for a periodic potential $U(x)$.[29] The solid line is a linear fit of eqn (8) to the data points with $\beta = 4.12$.

Because ν_1 contains the second derivatives of $U(x)$ at the potential minimum and maximum, information about $U(x)$ is still needed in order to accurately calculate ν_1. In a recent experiment, Ma *et al.*[29] measured the values of ν_1 for a periodic potential $U(x)$ with different barrier heights E_{b}. Fig. 1 shows the measured ν_1 as a function of $E_{\mathrm{b}}/k_{\mathrm{B}}T$. It is seen that the measured ν_1 is well described by a linear function

$$\nu_1 \simeq \beta\frac{E_{\mathrm{b}}}{k_{\mathrm{B}}T}, \tag{8}$$

with $\beta = 4.12$ (solid line). In fact, one can readily show that eqn (8) is valid for all the potentials with the scaling property $U(x) = ag(bx)$, where a and b are the scaling factors, and the shape of the function $g(x)$ determines the value of β.

For small values of $E_{\mathrm{b}}/k_{\mathrm{B}}T$, the steepest-descent approximation is not accurate, and the Arrhenius–Kramers equation was found to show deviations from the experimental results.[29] In this case, one can expand R_λ as a function of $U(x)/k_{\mathrm{B}}T$ and we find

$$\begin{aligned} R_\lambda &= e^{E_{\mathrm{b}}/k_{\mathrm{B}}T}\left\langle e^{[U(x)-E_{\max}]/k_{\mathrm{B}}T}\right\rangle_\lambda \left\langle e^{[E_{\min}-U(x)]/k_{\mathrm{B}}T}\right\rangle_\lambda \\ &\simeq \frac{1}{\nu_2}e^{E_{\mathrm{b}}/k_{\mathrm{B}}T}, \end{aligned} \tag{9}$$

where

$$\nu_2 = 1 + E_{\mathrm{b}}/k_{\mathrm{B}}T + (1/2 - c)(E_{\mathrm{b}}/k_{\mathrm{B}}T)^2 + \cdots \tag{10}$$

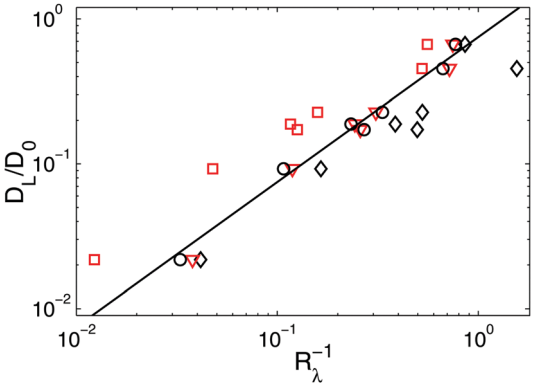

Fig. 2 Comparison between the measured D_L/D_0 and the calculated $1/R_\lambda$ under different approximations: (i) eqn (3) without any approximation (black circles), (ii) eqn (6) with ν_1 given in eqn (7) (black diamonds), (iii) eqn (9) with $\nu_2 = 1 + E_b/k_BT$ (red squares), and (iv) eqn (9) with $\nu_2 = 1 + E_b/k_BT + (3/8)(E_b/k_BT)^2$ (red triangles). The solid line is a plot of eqn (5) with $z = 3$.

In the above equation, $E_b = E_{max} - E_{min}$, and E_{max} and E_{min} are, respectively, the local maximum and minimum of the potential $U(x)$. In the expansion of the exponential functions in eqn (9), we used the relation $\langle U^2\rangle_\lambda - \langle U\rangle_\lambda^2 = cE_b^2$. For a sinusoidal potential $U(x) = U_0\cos(x/\lambda)$, one has $c = 1/8$, whereas for a square wave potential, we have $c = 1/4$. In general, we expect $0 \le c \le 1/4$. Except the numerical factor c, eqn (9) and (10) do not require information about the functional form of $U(x)$.

To examine the accuracy of the calculated R_λ under different approximations, we compare the theoretical predictions with the experimental results obtained for a periodic potential $U(x)$.[29] In the experiment, the functional form of $U(x)$ was accurately measured. Fig. 2 shows a comparison between the measured values of D_L/D_0 and the calculated values of $1/R_\lambda$ under different approximations. The black circles are obtained with the numerically calculated R_λ using eqn (3) and measured $U(x)$ without any approximation. The data are well described by eqn (5) with $z = 3$ for a hexagonal lattice (solid line). The black diamonds are obtained using the Arrhenius–Kramers equation [eqn (6)] and the numerically calculated ν_1 given in eqn (7). As expected, the Arrhenius–Kramers equation shows deviations from the exact result (solid line) for small values of E_b/k_BT (large values of $1/R_\lambda$), and the data approach the solid line at the largest value of $E_b/k_BT = 6.4$ studied.[29] The red squares and triangles are obtained using the same eqn (9) but with different orders of expansion for ν_2 [see eqn (10)]. The red squares are obtained with ν_2 being expanded to the first order of E_b/k_BT. The red triangles are obtained with ν_2 being expanded to the second order of E_b/k_BT (with $c = 1/8$). It is seen that the red squares are very close to the solid line for small values of E_b/k_BT (large values of $1/R_\lambda$) and deviations from the solid line become larger for large values of E_b/k_BT. With ν_2 being expanded to the second order of E_b/k_BT, we find that the red triangles are in good agreement with the solid line. Fig. 2 thus provides an overall evaluation of different theoretical approximations.

B. Colloidal diffusion over a random potential

For a 1D random potential, Zwanzig[16] showed that

$$D_L = \frac{D_0}{R_r}, \tag{11}$$

where $R_r = \langle e^{U(x)/k_BT}\rangle_r\langle e^{-U(x)/k_BT}\rangle_r$, and $\langle\cdots\rangle_r$ denotes an average over the random configurations. For the quenched 2D random potential to be discussed below (see Fig. 7 below), we generalize the above results and obtain

$$D_L = \frac{\bar{z}}{4}\frac{D_0}{R_X}, \tag{12}$$

where $\bar{z}$ is the mean number of the nearest neighbour sites, and the factor R_X is given by

$$R_X = \langle e^{U(X)/k_BT}\rangle_X\langle e^{-U(X)/k_BT}\rangle_X. \tag{13}$$

In the above equation $\langle\cdots\rangle_X$ denotes an average over all the quasi-1D paths X in the potential landscape (or "potential paths" for short) that the top diffusing particles have gone through. Fig. 13 below shows an example of such a potential path, which is a 1D numerical representation of the random potential field $U(x,y)$ that the particle has sampled. The hindering effect of the potential $U(X)$ on long-time diffusion is included in R_X.

To further simplify eqn (13), we divide the entire potential path X into N pieces, and each piece X_i contains only one local minimum and one local maximum of the potential. In this case, we have

$$\begin{aligned} R_X &\simeq \frac{1}{N}\sum_i^N \left\langle e^{U(X)/k_BT}\right\rangle_{X_i}\frac{1}{N}\sum_j^N\left\langle e^{-U(X)/k_BT}\right\rangle_{X_j} \\ &\simeq \frac{1}{N}\sum_i^N \left\langle e^{U(X)/k_BT}\right\rangle_{X_i}\left\langle e^{-U(X)/k_BT}\right\rangle_{X_i} \\ &\simeq \left\langle \frac{e^{E_b/k_BT}}{\nu_2(E_b)}\right\rangle_{E_b}, \end{aligned} \tag{14}$$

where

$$\left\langle \frac{e^{E_b/k_BT}}{\nu_2(E_b)}\right\rangle_{E_b} = \int\frac{e^{E_b/k_BT}}{\nu_2(E_b)}H(E_b)dE_b, \tag{15}$$

and $H(E_b)$ is the probability density function (PDF) of the barrier height E_b.

In writing the first equality, we have assumed that the path length X_i of each piece is approximately the same. This approximation is valid for the 2D random potential to be discussed below, in which the distance between any two nearest local minima of the potential does not vary much. To obtain the second equality, we have assumed that $\langle e^{U(X)/k_BT}\rangle_{X_i}$ and $\langle e^{-U(X)/k_BT}\rangle_{X_j}$ are statistically independent, so that the product of the two averages is equal to the average of their product. To verify this assumption, we calculate the normalized correlation coefficient C_N between the ith local potential maximum U^i_{max} and its

neighbouring jth local potential minimum $U^j_{\min}$ averaged along all the potential paths,

$$C_N = \frac{1}{N}\sum_{\{i,j\}}^{N} \frac{(U^i_{\max} - \overline{U}_{\max})(U^j_{\min} - \overline{U}_{\min})}{\delta U_{\max}\delta U_{\min}}, \quad (16)$$

where $\bar{U}_{\max}$ ($\bar{U}_{\min}$) and $\delta U_{\max}$ ($\delta U_{\min}$) are, respectively, the mean value and the standard deviation of $U^i_{\max}$ ($U^j_{\min}$). In the above, only the neighbouring pairs $\{i,j\}$ are taken in the average. In this way, C_N becomes significantly non-zero only when the fluctuations of the local potential maximum $U^i_{\max}$ relative to its mean value $\bar{U}_{\max}$ are correlated with the fluctuations of the neighbouring local potential minimum $U^j_{\min}$. It is found that the correlation coefficient is actually very small with $C_N \simeq 0.01$. Because the values of $\langle e^{U(X)/k_BT}\rangle_{X_i}$ and $\langle e^{-U(X)/k_BT}\rangle_{X_j}$ are determined primarily by the local maximum and minimum, respectively, in each potential path, the small value of C_N indicates that the two quantities are essentially independent. The last equality in eqn (14) is obtained using the results in eqn (9).

Substituting eqn (14) into eqn (12), we have

$$D_L = \frac{\bar{z}}{4}\frac{D_0}{\left\langle \frac{e^{E_b/k_BT}}{\nu_2(E_b)}\right\rangle_{E_b}}. \quad (17)$$

In Section IVB2 below, we will compare the experimental results with the predictions given by eqn (12) and (17).

III. Experiment

The experimental apparatus and procedures used in this experiment are similar to those described previously,[29,32] and here we mention only some key points. Fig. 3 shows the sample cell used in the experiment. It has a circular stainless steel chamber (SC) with a central hole of 8 mm in diameter and 1 mm in depth, which is sealed from the bottom by a glass cover slip (GC). The central hole is first filled with the colloidal sample and extra solvent (water) is added to fill the entire sample cell. After filling the fluid chamber, another glass cover slip (GC) is used to cover the entire sample cell. In this way, both sample evaporation and unwanted flow are minimized.

Plain silica spheres purchased from Bangs Laboratories are used in the experiment. They are cleaned prior to use following the same procedure as described in ref. 29. To make a 2D disordered potential field, we use a mixture of bidisperse silica spheres to form a randomly packed colloidal monolayer on the bottom glass slide. There are two control parameters for the binary mixture: the particle size ratio d_L/d_S and the area ratio n_L/n_S. In addition, the total area fraction $n_b = n_L + n_S$ determines how close the mixture is packed. Here we used the subscripts L and S to indicate the large and small spheres, respectively. In the experiment, one can vary n_L/n_S (and n_b) to obtain different particle configurations, including both the well-mixed (homogenous) states and those states with micro-structures.[39–41] This method thus provides a well-controlled and convenient way to vary the 2D potential field with different disorders.

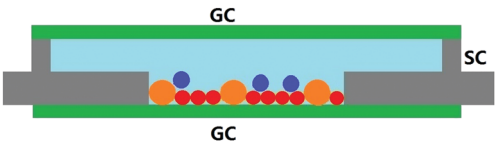

Fig. 3 Schematic diagram of the sample cell (side view): SC, stainless steel chamber; GC, glass cover slip; orange and red particles, bidispersed silica spheres forming a randomly packed colloidal monolayer on the bottom glass substrate; blue particles, silica spheres of a different size diffusing on top of the randomly packed colloidal monolayer.

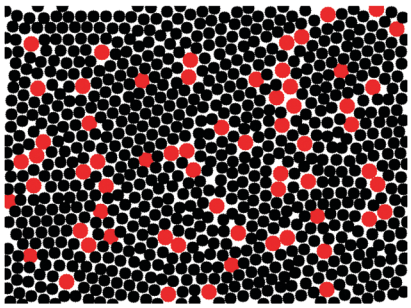

Fig. 4 Particle configuration of the bottom layer particles at a relatively well-mixed state with d_L = 2.94 μm (red dots), d_S = 2.47 μm (black dots), n_L/n_S = 0.16, and $n_b \simeq 0.8$.

Hereafter, we report the experimental results obtained using a fixed binary mixture of silica spheres with d_S = 2.47 μm, d_L = 2.94 μm, and n_L/n_S = 0.16. This system is chosen in order to obtain a well-mixed (homogeneous) particle configuration without visible crystal patches of either size of particles. Fig. 4 shows the particle configuration of a relatively well-mixed state of the silica sphere mixture. In the experiment, we prepare the binary mixture with its concentration adjusted so that when the suspension is filled into the central hole ($\sim$50 μL in volume) of the fluid chamber, the particles settle on the glass substrate under gravity and form a closely packed monolayer with $n_b \simeq 0.8$. The sample is then left open for complete evaporation of water in the solution and the remaining particles are attached to the glass substrate by van der Waals forces. After the formation of the fixed bottom monolayer of the silica spheres on the substrate, we fill the central hole with a different suspension of monodispersed silica spheres with a desired concentration. It takes several minutes for the silica spheres to settle down on top of the bottom layer of the randomly packed particles.

The top layer particles diffuse over a rugged surface formed by the bottom colloidal layer and experience a gravitational potential $U(x,y)$. The values of $U(x,y)$ are determined by the size of the silica spheres in both layers.[29] There is a small gap between the two layers of silica spheres, which affects both the diffusion dynamics of the particles in the top layer and the potential field $U(x,y)$. To obtain consistent experimental results, we add 0.1 mM NaCl into the water to control the Debye screening length of the silica spheres so that the gap distance remains constant. To vary $U(x,y)$, we change the size of the top layer silica spheres, whereas the bottom layer of the randomly packed particles remains unchanged. The dynamical properties

of the top layer particles are obtained in the dilute limit with the area fraction n_t occupied by the top layer particles set at $n_t \simeq 0.05$. A similar area fraction was used in a previous study of colloidal diffusion over the periodic potentials.[29,32]

To obtain the occupation statistics of the top layer particles and find the potential $U(x,y)$, a higher area fraction $n_t \lesssim 0.3$ is used. In the previous study of colloidal diffusion over the periodic potentials,[29] two area fractions, $n_t = 0.15$ and $n_t = 0.3$, were used to measure the population probability histogram (PPH) $P(x,y)$ of finding a diffusing particle at a location (x,y). No visible difference was found in the two measured PPHs. A lower area fraction, $n_t = 0.15$, was used for the periodic potentials, as an additional spatial average over the unit cell of the lattice was used to improve the statistics of the measured $P(x,y)$. For random potentials, however, this spatial periodicity is not available and a higher area fraction, $n_t \lesssim 0.3$, is used to improve the statistics of $P(x,y)$. The interaction between the silica spheres used here can be well described by a hard-sphere-like potential with the interaction range $r \lesssim 1.1d$.[33] This value of r is smaller than the mean particle separation, $\ell \simeq d[\pi/(4n)]^{1/2} \simeq 1.62d$ for $n_t = 0.3$, indicating that the interaction effect on $P(x,y)$ is small and can be neglected in this case. Six colloidal samples with different particle sizes are used in the experiment, and their properties are given in Table 1.

The sample cell is placed on the stage of an inverted microscope (Olympus IX71). The motion of the top-layer diffusing particles is viewed from below using bright field microscopy and recorded using a CCD camera (CoolSNAP, Media Cybernetics). Before each movie taking, the level of the microscope/sample is carefully adjusted to eliminate small drifts of the diffusing particles, and adequate time ($\sim$1 h) is given to allow the sample to reach equilibrium. Typically, each movie lasts for 2 h at a frame rate 7 frames per second (fps). The recorded images have a spatial resolution of 1392 $\times$ 1040 pixels and 4096 gray scales. A homemade program based on the standard tracking algorithm[42] is used to find the trajectory of the diffusing particles from consecutive images. With this program we are able to obtain a tracking accuracy of 1 pixel $\simeq$ 109 nm. More details about the image processing were given in ref. 29.

Table 1 Six colloidal samples used in the experiment with different diameters d_t for the top layer particles. Also shown are the normalized long-time diffusion coefficient D_L/D_0 and the potential landscape parameters, including the mean value of the barrier height $\langle E_b \rangle$, the numerically calculated values of $[R_X^{-1}]_1$ using eqn (13) and $[R_X^{-1}]_2$ using eqn (14). These quantities are obtained in the present experiment

Sample	d_t (μm)	D_L/D_0	$\langle E_b \rangle/k_BT$	$[R_X^{-1}]_1$	$[R_X^{-1}]_2$
S1	1.57	0.59	0.93	1.42	1.48
S2	1.85	0.58	0.95	1.38	1.48
S2[a]	1.85	0.63	0.96	1.37	1.48
S3	2.01	0.55	1.08	1.66	1.66
S3[a]	2.01	0.52	1.11	1.63	1.71
S4	2.14	0.43	1.28	1.96	2.02
S4[a]	2.14	0.39	1.34	1.97	2.15
S5	2.47	0.29	1.60	3.26	2.99
S6	2.94	0.061	2.50	10.86	11.45

[a] Results obtained from a different measurement of the same sample.

IV. Experimental results

A. Quenched 2D random potential

We obtain the PPH $P(x,y)$ by counting the occupation number of the top layer particles within each pixel from two movies, each containing (4–6) $\times$ 10^4 frames. The two movies contain 6×10^7 particles in total. Fig. 5 shows a 3D plot of the measured $P(x,y)$ over a large area for sample S3. In the plot, $P(x,y)$ is not normalized so that one can directly see the number statistics. The peak positions of the measured $P(x,y)$ locate at the interstices of the bottom particles. The valley regions in the measured $P(x,y)$ correspond to the top of the bottom particles. The shape and symmetry of the measured $P(x,y)$ reflect the topographic variations of the underlying rugged surface. We also find a number of fluctuations in the measured $P(x,y)$, which are caused by the limited statistics of the particles in certain locations. The relative error $\sigma(x,y)$ of the measured $P(x,y)$ can be estimated as $\sigma(x,y) = [n_i(x,y)]^{-1/2}$, where $n_i(x,y)$ is the number of particles counted in the ith pixel. Typically, we have $\sigma_{peak} \simeq 10\%$ in the peak region and $\sigma_{valley} \simeq 20\%$ in the valley region of $P(x,y)$, which corresponds to an energy uncertainty of $\pm 0.2\ k_BT$.

The measured $P(x,y)$ is related to the potential $U(x,y)$ by the Boltzmann distribution,

$$P(x,y) \sim e^{-U(x,y)/k_BT}. \quad (18)$$

With eqn (18) we calculate the 2D potential, $U(x,y)/k_BT = -\ln P(x,y)$, where a normalization factor is chosen for $P(x,y)$ so that $U(x,y) = 0$ at the lowest potential minimum. Fig. 6 shows a 3D plot of the resulting $U(x,y)/k_BT$ for sample S1. The unit of x and y has been converted from pixel to micrometer using 1 pixel = 109 nm for our microscope setup. Compared to 1D random fields, the 2D colloidal landscape provides a larger sampling area, better particle statistics, and a longer time at equilibrium for the diffusing particles to explore different energy configurations without being overwhelmingly trapped to some deep potential minima.

A homemade programme is used to divide the obtained 2D potential field into different states, which are defined by the yellow polygons as shown in Fig. 7. Each of the polygons is

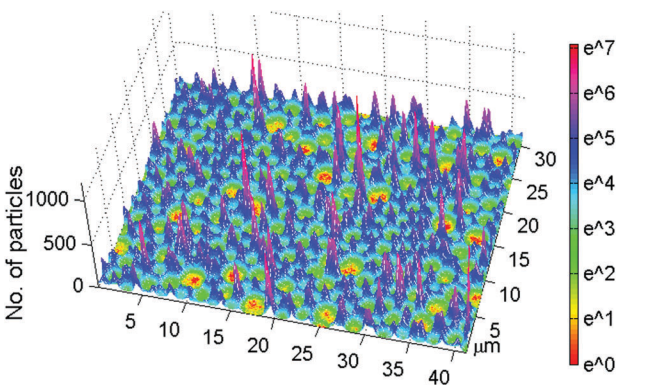

Fig. 5 3D plot of the measured PPH $P(x,y)$ for sample S3. The PPH is not normalized and the height shows the number statistics in each pixel. The color bar indicates the scale of $\ln P(x,y)$.

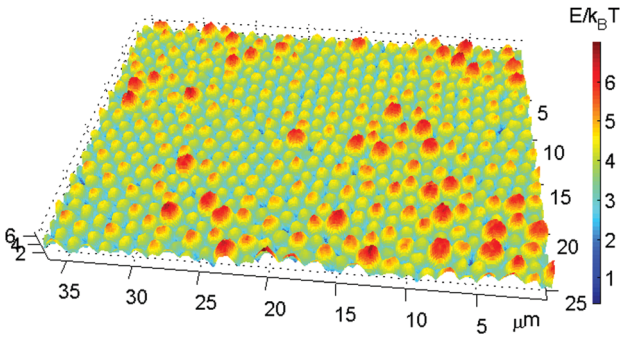

Fig. 6 3D plot of the obtained potential field, $U(x,y)/k_BT = -\ln P(x,y)$, for sample S1.

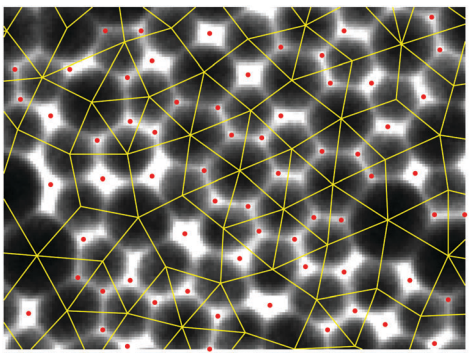

Fig. 7 Top view of the 2D random potential field for sample S1. The background is a 2D plot of the measured $P(x,y)$ in gray-scale. Brighter regions are the lower potential regions. The red dots indicate the location of the potential minima (traps), which are the peak positions of the measured $P(x,y)$. The yellow polygons divide the 2D potential field into different states, each has a potential trap located at its center.

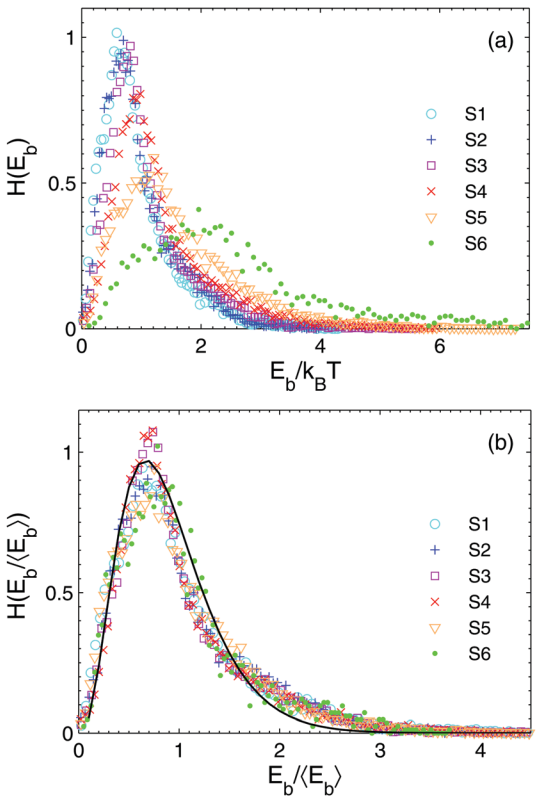

Fig. 8 (a) Measured histogram $H(E_b)$ of the barrier height E_b for six colloidal samples. (b) Measured histogram $H(E_b/\langle E_b\rangle)$ as a function of the normalized barrier height $E_b/\langle E_b\rangle$, where $\langle E_b\rangle$ is the mean value of E_b. The data are the same as those shown in (a). The solid line shows the gamma distribution in eqn (19) with $\alpha_1 = 3.8$ and $\alpha_2 = 4.2$.

centred around a peak of the measured $P(x,y)$ (red dots), which is a local minimum of $U(x,y)$ and serves as a trap to the diffusing particles. The boundaries of the polygon are defined by the intersecting lines, which connect the centres of two adjacent bottom particles. There is a potential ridge between two adjacent traps (red dots), and it has a local maximum (saddle point) of the potential $U(x,y)$. The potential difference between a local potential minimum and its nearby saddle point defines the energy barrier E_b. The diffusing particles in each trap need to cross an energy barrier in order to move to a different state. With the construction as shown in Fig. 7, one can convert the particle trajectories in position to the potential paths of the numbered states that the diffusing particles have gone through. There are some locations in the viewing area, which the diffusing particles have never visited. These unvisited locations, however, do not affect the results presented below, as the ensemble averages used below are all based on the particle's paths and the unvisited locations are simply not included in the ensemble averages.

Because the potential field is random, the obtained values of E_b vary among different locations. Fig. 8(a) shows the normalized histogram [or probability density function (PDF)] $H(E_b)$ of the measured barrier height E_b for six different samples. Because the potential energy of the top diffusing particles is proportional to its own volume d_t^3,[29] the measured $H(E_b)$ extends toward large values of E_b for bigger particles. Nonetheless, all of the measured $H(E_b)$ curves collapse onto a single master curve, as shown in Fig. 8(b), once E_b is normalized by its own mean value $\langle E_b\rangle$ (see Table 1). Thus the functional form of $H(E_b/\langle E_b\rangle)$ is determined uniquely by the configuration of the bottom layer particles and is independent of the size of the top layer particles. The shape of the measured $H(E_b/\langle E_b\rangle)$ is asymmetric with a long tail for large values of $E_b/\langle E_b\rangle$ and can be approximately described by an empirical function of gamma distribution,

$$H(E_b/\langle E_b\rangle) = \frac{(\alpha_2)^{\alpha_1}}{\Gamma(\alpha_1)}\left(\frac{E_b}{\langle E_b\rangle}\right)^{\alpha_1-1} e^{-\alpha_2(E_b/\langle E_b\rangle)}, \quad (19)$$

with $\alpha_1 = 3.8$ and $\alpha_2 = 4.2$ (solid line).

B. Diffusion dynamics over the quenched 2D random potential

1. Escape time t_E and its distribution. From the particle trajectories, we find that the particles spend most of their time diffusing around local minima of the potential. Only after a long time t_E, they will escape to a nearby potential minimum. Hereafter, we call the potential minima as traps. As shown in Fig. 7, we convert the particle trajectories in position to the

potential paths of the numbered states and measure the escape time t_E for each trap, which is the time that the particle has stayed before crossing the boundary of the trap. Special care is taken to those trajectories starting from or arriving at the immediate neighbourhood of the boundaries. A new state is assigned only after the particle has crossed the boundary and moved away from it over a specified distance (typically 10% of the distance between the two nearby traps). By doing so, those rapid crossings of the boundary due to thermal fluctuations are not counted in the measured t_E. Fig. 9(a) shows the measured histogram $P(t_E)$ of the escape time t_E for sample S3[a] (blue line). It has a shape similar to a stretched exponential function.

As shown in Fig. 8, our 2D potential has many traps of different barrier heights, which give rise to a distribution $f(\bar{t}_E)$ of the mean escape time (or residence time) $\bar{t}_E$ associated with each trap. Notice that $\bar{t}_E$ is related to MFPT $\bar{t}_1$ in eqn (4) *via* $\bar{t}_E = \bar{t}_1/z$,[34] if each trap has z nearest neighbor traps of equal energy barrier E_b. Fig. 9(b) shows the measured histogram $f(\bar{t}_E)$ for sample S3[a]. It has a dominant peak and a small and broad secondary peak in the tail part of the measured $f(\bar{t}_E)$. The measured $f(\bar{t}_E)$ for other samples has a similar shape. It is seen from Fig. 7 that the trap regions (bright areas) in the potential field can be roughly divided into two groups. One group is shallow and small with its local structure not deviated very much from the crystal structure. The other group is much deeper and larger resulting from the large mismatched structures. These two groups of potential traps give rise to the two peaks in the measured $f(\bar{t}_E)$. The two arrows in Fig. 9(b) indicate the range of the measured $f(\bar{t}_E)$ with continuous non-zero values of $\bar{t}_E$ above the noise background.

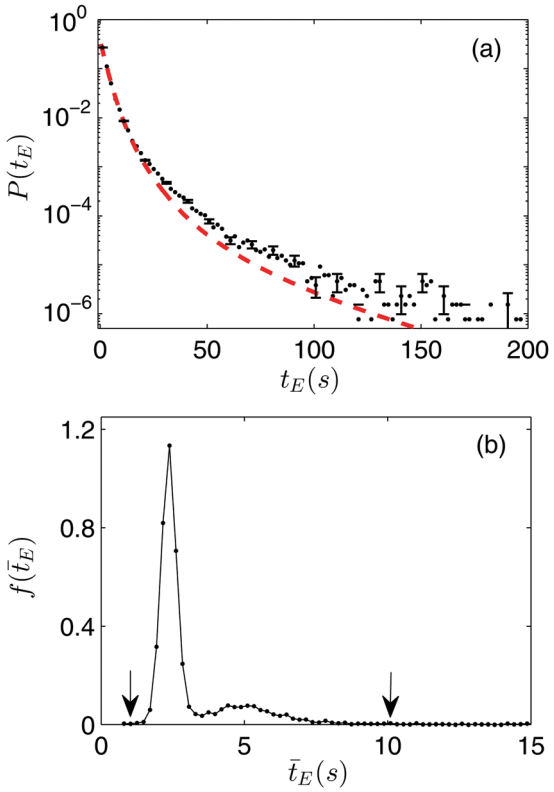

Fig. 9 (a) Measured histogram $P(t_E)$ of the escape time t_E for sample S3[a] (black dots). The error bars indicate the standard deviation of the measurements. The red dashed line shows the numerically calculated $P(t_E)$ using eqn (20). (b) Measured histogram $f(\bar{t}_E)$ of the mean escape time $\bar{t}_E$ for sample S3[a]. The two arrows point to the locations of the minimal value $(\bar{t}_E)_{min}$ (left arrow) and maximal value $(\bar{t}_E)_{max}$ (right arrow) of the measured $\bar{t}_E$.

For a single barrier with a large enough value of E_b/k_BT, t_E obeys the simple exponential distribution with a constant escape rate.[34] The total distribution $P(t_E)$ can be written as a superposition of different exponential distributions weighted by the measured $f(\bar{t}_E)$,

$$P(t_E) = \int f(\bar{t}_E)\frac{1}{\bar{t}_E}e^{-t_E/\bar{t}_E}d\bar{t}_E. \quad (20)$$

The red dashed line in Fig. 9(a) shows the numerically calculated $P(t_E)$ using eqn (20) and measured $f(\bar{t}_E)$. The calculated $P(t_E)$ overlaps well with the measured $P(t_E)$ at small values of t_E over almost three orders of magnitude. While the difference between the two curves is comparable to the scatters of the measurement, there are two sources of error which may contribute to the small but systematic deviations at large values of t_E. One is the statistical error of the measured histogram, which is inversely proportional to the total counts in each bin of the histogram. This error causes the histogram to level off for $t_E \gtrsim 100$ s. The other source of error comes from the fact that for small energy barriers, the distribution of the escape time t_E from a single barrier may not be a simple exponential function, as assumed in eqn (20). Because there is no clear time separation in this case, the escape events cannot be treated as a Poisson process any more.

For our 2D random potential, a single trap may have several exits of different barrier heights. The measured mean escape rate $1/\bar{t}_E$ from the trap is a sum of the individual escape rates $1/(\bar{t}_E)_i$ across the ith exit. Therefore, one can estimate the value of the escape time $(\bar{t}_E)_i$ for particles to cross a single exit of barrier height $(E_b)_i$ as

$$(\bar{t}_E)_i \simeq \frac{m}{m_i}\bar{t}_E, \quad (21)$$

where m_i is the number of escape events across the ith barrier and m is the total number of escape events from the trap. In the experiment, we follow the particle's potential paths and obtain the values of m_i, m, $\bar{t}_E$, $(E_b)_i$, and the distance λ_i between the two nearby traps across the energy barrier $(E_b)_i$. Fig. 10 shows the obtained individual escape rate $(\bar{t}_E)_i/(t_0)_i$ as a function of barrier height $(E_b)_i/k_BT$ (orange dots). In the plot, $(\bar{t}_E)_i$ is normalized by the free diffusion time $(t_0)_i = (\lambda_i/2)^2/D_0$ over the lateral distance $\lambda_i/2$ between the potential minimum and its nearby maximum. Because the number statistics of the escape events across each exit is quite limited, the data points scatter considerably. Nonetheless, after a running average of all the data points from the six colloidal samples, we obtain a smooth curve of $(\bar{t}_E)_i/(t_0)_i$ (black curve).

For large values of E_b/k_BT, eqn (4), (6) and (8) are valid, and we find they fit the data well in the region $E_b/k_BT \gtrsim 3$ with the fitting parameter $\beta \simeq 4.12$ (blue dashed line). For shallow traps

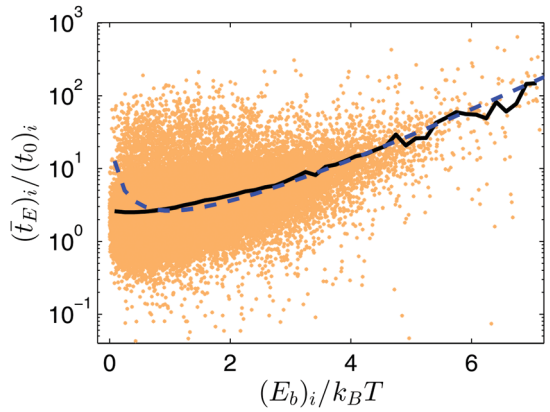

Fig. 10 Measured individual escape rate $(\bar{t}_E)_i/(t_0)_i$ as a function of barrier height $(E_b)_i/k_BT$ (orange dots). The data points are obtained from all the six colloidal samples. The black curve shows the average value of the orange dots. The blue dashed line is a fit of eqn (6) and (8) to the data points in the region $E_b/k_BT \geq 3$ with the fitting parameter $\beta \simeq 4.12$.

with $E_b/k_BT \lesssim 2$, we find deviations between the two curves. In this case, eqn (6) and (8) are no longer valid. In addition, the mean escape time $\bar{t}_E$ (or MFPT $\bar{t}_1$) is not well defined in the experiment, as it depends sensitively on the beginning and ending points of the particle trajectories. For example, the MFPT $\bar{t}_1$ in eqn (4) is defined as the time for a particle to move from the center of a trap to a nearby center of the trap. When the potential barrier is large enough, $\bar{t}_1$ (or $\bar{t}_E$) is determined primarily by the waiting time for the particle to cross over the potential barrier. The shallow traps will not affect the determination of D_L in eqn (1), as it is measured over a time much longer than $\bar{t}_E$ (see more discussions below).

2. Mean square displacement and long-time diffusion. From the particle trajectories, one can also calculate the MSD $\langle \Delta \mathbf{r}^2(\tau) \rangle$ as a function of delay time τ. Fig. 11 shows log–log plots of the measured MSD $\langle \Delta \mathbf{r}^2(\tau) \rangle$ as a function of τ for six colloidal samples. The measured MSD curves can be generally described by[7,8]

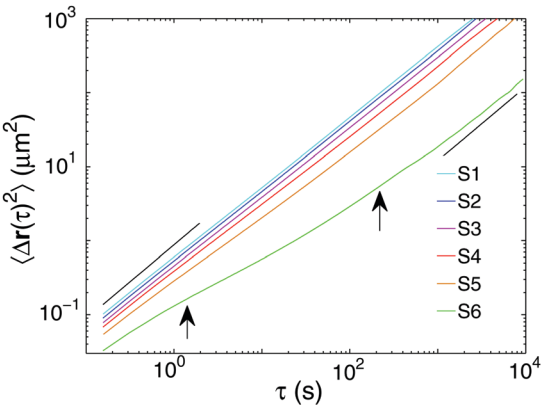

Fig. 11 log–log plots of the measured MSD $\langle \Delta \mathbf{r}^2(\tau) \rangle$ as a function of delay time τ for six colloidal samples. The black solid lines indicate the relationship $\langle \Delta \mathbf{r}^2(\tau) \rangle \sim \tau$ with a slope of unity in the log–log plot. The two arrows point to the locations of $(\bar{t}_E)_{min}$ (left arrow) and $(\bar{t}_E)_{max}$ (right arrow), respectively, for sample S6.

$$\langle \Delta \mathbf{r}^2(\tau) \rangle \sim \tau^{\gamma}, \quad (22)$$

where the exponent γ is used to classify the particle's motion as normal diffusion ($\gamma = 1$), sub-diffusion ($\gamma < 1$) or super-diffusion ($\gamma > 1$). It is found that for short delay times with $\tau < (\bar{t}_E)_{min}$, most particles rattle around the potential minima and their motion is diffusive with $\gamma = 1$ (lower left solid line). At long delay times with $\tau > (\bar{t}_E)_{max}$, the particles have experienced (or hopped over) many potential barriers, and their trajectories are randomized without much correlation (see Fig. 9(b) for the definition of $(\bar{t}_E)_{min}$ and $(\bar{t}_E)_{max}$). In this case, we find that the measured MSD $\langle \Delta \mathbf{r}^2(\tau) \rangle$ obeys eqn (1) (upper right solid line), from which we obtain the long-time diffusion coefficient D_L.

In the crossover region $(\bar{t}_E)_{min} \lesssim \tau \lesssim (\bar{t}_E)_{max}$, the particle's motion becomes heterogeneous and undergoes anomalous subdiffusion with $\gamma < 1$. By comparing the measured MSD curves from different samples, we find that the anomalous subdiffusion becomes more pronounced for the colloidal samples with a larger value of E_b and with a wider distribution of $\bar{t}_E$. The two arrows in Fig. 11 indicate the range of the measured $\bar{t}_E$ for sample S6. In this case, the trajectory randomization time τ_L for the measured $\langle \Delta \mathbf{r}^2(\tau) \rangle$ to become diffusive again is increased to more than 5 times larger than the measured $(\bar{t}_E)_{max}$. This is very different from the situation for a period potential, in which case the measured MSD becomes diffusive right after $\bar{t}_E$ (*i.e.*, $\tau_L \simeq \bar{t}_E$).[29] Such a crossover behavior of MSD has been observed previously for colloidal diffusion over the random potentials generated by holographic optics.[26,27] It was also observed in dense fluid systems, such as colloidal diffusion near its glass transition.[43,44] Membrane proteins in live cells were also found to exhibit anomalous subdiffusion.[13,14] Further analysis on anomalous subdiffusion will be given in the next section.

The measured values of D_L are shown in Table 1, which indicates that D_L decreases with the mean barrier height $\langle E_b \rangle$. When compared with the periodic potential with similar values of the barrier height,[29] we find that the quenched randomness of the potential significantly reduces the diffusion rate. This suggests that the long tail portion of the measured barrier height distribution $H(E_b)$, as shown in Fig. 8, serves as a kind of bottle-neck for determining the long-time diffusion behaviour. We now test the theoretical predictions for long-time diffusion constant D_L. Fig. 12 shows a comparison between the measured values of D_L/D_0 and the calculated values of $1/R_X$. The black circles are obtained with the numerically calculated R_X using eqn (13) and the potential $U(X)$ obtained from the $n = 0.05$ sample without further approximation. The data are well described by eqn (12) with the mean number of the nearest neighbour sites $\bar{z} = 3.4$ (solid line). The obtained value of $\bar{z}$ from direct counting of the 2D potential $U(x,y)$ is $\bar{z} = 3.3 \pm 0.13$, which agrees with the above fitted value within the experimental uncertainties.

Because a particle stays in a deep trap for a longer period of time, its occupation may affect the probability for other particles to visit the occupied site at high particle concentrations. To further examine the concentration effect, we compute R_X again

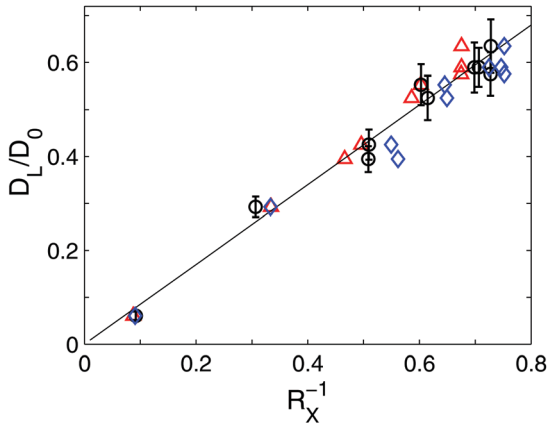

Fig. 12 Comparison between the measured D_L/D_0 and calculated $1/R_X$ under different approximations: (i) eqn (13) together with the potential $U(X)$ obtained from the n = 0.05 sample without further approximation (black circles), (ii) eqn (13) together with the potential $U(X)$ obtained from the n = 0.3 sample without further approximation (blue diamonds), and (iii) eqn (14) with $\nu_2 = 1 + E_b/k_BT$ (red triangles). The error bars show the experimental uncertainties of the measured D_L/D_0. The solid line is a linear fit of eqn (17) to the black circles with $\bar{z}$ = 3.4.

using the potential $U(x,y)$ obtained from the concentrated sample (n = 0.3). The blue diamonds in Fig. 12 show the high concentration results. While there are some slight differences between the black circles and blue diamonds, Fig. 12 confirms that these differences are negligibly small. With this experimental verification, we used the potential $U(x,y)$ obtained from the n = 0.3 sample for the data analyses shown in Fig. 6–10, to further improve the statistical accuracy and reduce the sampling errors.

In the calculation of R_X in eqn (13), the average $\langle\cdots\rangle_X$ is conducted over all the "path area" occupied by the potential paths that the particles have gone through. Fig. 13(a) shows an example of a 20 min-long single-particle trajectory (green curve), which is superimposed on the measured $P(x,y)$ in gray scale. It is seen that the particle spends most time in the low-potential regions (white areas). The path area is defined when the value of the measured $P(x,y)$ becomes larger than a threshold value P_c, which is carefully chosen for each sample to ensure that the fraction of the path area visited by the particles is approximately the same for all the samples (typically 62.5% of the view area). For sample S1, we set the highest threshold P_c, under which there are still more than 90% of the particle trajectories located in the path area. With this definition, we find that most of the particle trajectories follow a narrow path over the 2D potential, so that our assumption about the quasi-1D potential paths is justified. In this way, we effectively ignored those areas in the 2D random potential, which the particles never or seldom visit.

Fig. 13(b) shows an example of the potential path $U(X)$ along a segment of the quasi-1D trajectories that the particle has gone through, as marked by the red lines in Fig. 13(a). With the above definition of the path area, the average $\langle\cdots\rangle_X$ in eqn (13) becomes

$$\langle e^{U(X)/k_BT}\rangle_X = \langle\langle e^{U(X,Y)/k_BT}\rangle_Y\rangle_X, \qquad (23)$$

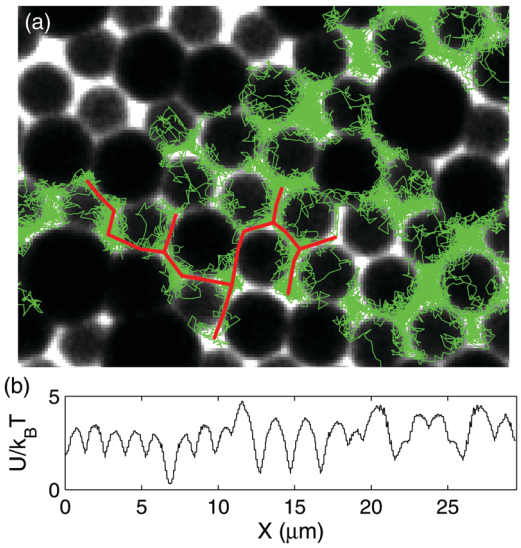

Fig. 13 (a) Measured 20 min-long trajectory (green curve) of a diffusing particle over a quenched 2D random potential for sample S5. The background is a 2D plot of the measured $P(x,y)$ in gray-scale with white areas indicating the low-potential regions. (b) An example of the potential path $U(X)$ along a segment of the quasi-1D trajectories that the particle has gone through [red lines marked in (a)].

where the average $\langle\cdots\rangle_Y$ is conducted over the "width" of the quasi-1D potential path inside the path area.

To check the validity of eqn (17), we numerically calculate the average $\langle\cdots\rangle_{E_b}$ in eqn (14) using the measured $H(E_b)$ as shown in Fig. 8. Because the measured $H(E_b)$ is concentrated mainly in the small-E_b range (0–2)k_BT, we choose $\nu_2 = 1 + E_b/k_BT$. The final results are shown in Fig. 12 (red triangles) and the numerical values of R_X^{-1} obtained in the two different ways are given in Table 1. It is seen that the red triangles are in good agreement with the theoretical prediction given in eqn (17). Fig. 12 thus provides a direct experimental support for the theoretical modeling discussed in Section IIB.

3. Further analysis of anomalous subdiffusion. To further understand the crossover behaviour and anomalous scaling in the subdiffusion regime, we compute additional statistical quantities from the measured particle trajectories. The first quantity is the non-Gaussian parameter $K(\tau)$, which is defined as

$$K(\tau) = 2\frac{\langle\Delta\mathbf{r}^4(\tau)\rangle}{\langle\Delta\mathbf{r}^2(\tau)\rangle^2} - 4 = \frac{\langle\Delta x^4(\tau)\rangle}{\langle\Delta x^2(\tau)\rangle^2} - 3. \qquad (24)$$

For normal diffusion, the displacement $\Delta x(\tau)$ follows the Gaussian statistics for all delay times τ, which gives rise to a vanishing $K(\tau)$. Fig. 14 shows the obtained $K(\tau)$ as a function of τ for three representative samples with low, intermediate and high energy barriers, respectively. It is seen that the measured $K(\tau)$ shows a broad peak with its maximal value located in the middle range of the crossover region. The value of $K(\tau)$ decays toward zero both in the short-time and long-time limits, in which the measured MSDs show normal diffusion. For samples with larger values of $\langle E_b\rangle$, the amplitude of their non-Gaussian peak increases with $\langle E_b\rangle$ and the peak position shifts toward larger values of τ.

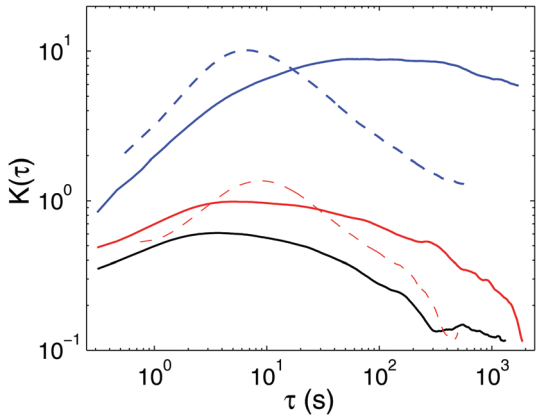

Fig. 14 Measured non-Gaussian parameter $K(\tau)$ as a function of delay time τ for samples S1 (black solid line), S4 (red solid line), and S6 (blue solid line). The red and blue dashed lines show, respectively, the measured $K(\tau)$ for particles diffusing over a periodic potential with barrier heights $E_b = 1.6k_BT$ and $E_b = 4.8k_BT$ (samples S2 and S6 in ref. 29).

Because $K(\tau)$ involves the fourth moment of $\Delta\mathbf{r}(\tau)$, it is more sensitive to the statistical noise compared to the MSD $\langle\Delta\mathbf{r}^2(\tau)\rangle$. For long delay times in the range $10^3\ s \lesssim \tau \lesssim 10^4$ s, the sample statistics is reduced considerably and we can only obtain reliable MSD curves, as shown in Fig. 11, but not $K(\tau)$ for sample S6. As a result, the measured $K(\tau)$ for sample S6 has not reached the diffusion limit yet ($K(\tau) = 0$).

For comparison, we also show, in Fig. 14, the measured $K(\tau)$ for particles diffusing over a periodic potential with a single value of barrier height E_b (dashed lines). In this case, the measured $K(\tau)$ shows similar features to those for the random potential, except that the width of the non-Gaussian peak is narrowed considerably. By comparing the values of the barrier height involved in both cases, we find that the range of the crossover regime for the random potential is determined primarily by the long tail part of the barrier height distribution $H(E_b)$, as shown in Fig. 8.

We now compare our results with the predictions of the Lorentz model,[45] which considered tracer diffusion through a heterogeneous space filled with a (fixed) set of randomly distributed obstacles. The diffusion dynamics in a heterogeneous space is determined by two aspects of the underlying structure.[46] One is how the accessible space $s(\ell)$ for diffusion over varying lengths ℓ is embedded in the physical space, which is characterized by the fractal dimension d_f as $s(\ell) \propto \ell^{d_f}$. The other aspect is how the accessible space $s(\ell)$ is visited by the random walkers, which is described by the relation $s(\ell) \propto \tau^{\delta}$. Combining these two aspects, one finds $\ell \propto \tau^{\delta/d_f} \equiv \tau^{\gamma/2}$, where γ is the subdiffusion exponent in eqn (22).

In the Lorentz model, when the density ρ of the obstacles becomes larger than a critical value ρ_c, the void space where the tracers are allowed to diffuse through decomposes into clusters of varying (finite) size ℓ. The correlation length ξ is defined as the linear dimension of the largest finite void cluster, which diverges when ρ approaches ρ_c. In this case, the tracers will all be trapped in some clusters of size ℓ. The void space thus can be thought of as a percolating space with a fractal dimension $d_f = 91/48$ for 2D.[47,48] When a tracer diffuses in a fractal space, it has a higher probability to encounter the forbidden region occupied by the obstacles with increasing displacement (or delay time τ). As a result, the tracer motion is slowed down with increasing τ, making it subdiffusive with the exponent $\gamma = 0.695$ based on the percolation theory.[48]

When $\rho < \rho_c$, the void clusters remain infinite but they are fractal with the same values of d_f and γ only for the sizes up to $\ell < \xi$. For larger length scales, the void space becomes homogeneous with $d_f = d$, where d is the dimension of the embedded space. In this case, tracer diffusion will have a crossover from subdiffusion to normal diffusion at $\ell_c \simeq \xi$.[49] To analyse the fractal structure of the 2D random potential field, we use the path area occupied by the potential paths that the particles have gone through as the void area. The definition of the path area has been described in Section IVB2. We then use the standard "mass-radius method"[50] to compute the fractal dimension d_f of the void area,

$$\rho(\ell) = \frac{s(\ell)}{\ell^2} \simeq \ell^{d_f-2}, \tag{25}$$

where $s(\ell)$ is the occupied path area in the box of varying size ℓ. In the calculation, a number of boxes centered at different positions in the path area are used to obtain an average value of $s(\ell)$.

Fig. 15 shows the obtained density $\rho(\ell)$ of the void area as a function of box size ℓ for 4 different samples. Within the experimental uncertainties, all the curves overlap with each other, as the underlying random field remains unchanged for all the samples. In the scaling range $\ell_0 \lesssim \ell \lesssim \ell_c$, the data can be well described by eqn (25) with $d_f = 1.83 \pm 0.02$. This value of d_f is very close to the predicted value $d_f = 91/48$ by the Lorentz model. As shown in Fig. 15, the lower cutoff length $\ell_0 \simeq 1$ μm, which is approximately the radius of the bottom layer particles. The upper cutoff length is $\ell_c \simeq 7$ μm, above which $\rho(\ell)$ is a constant and hence the void area becomes homogeneous with

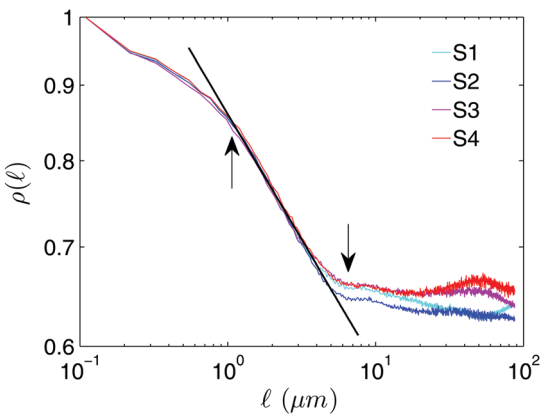

Fig. 15 Obtained density $\rho(\ell)$ of the void area as a function of box size ℓ for 4 different samples S1–S4. The black line is a fit to eqn (25) with $d_f = 1.83 \pm 0.02$. The arrows indicate the scaling range of the (fractal) void area with ℓ_0 and ℓ_c being, respectively, the lower and higher cutoff lengths.

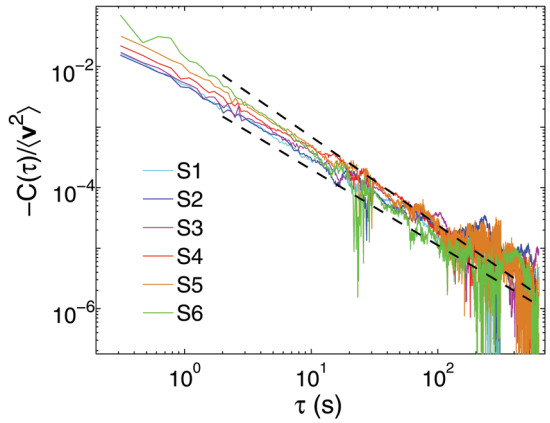

Fig. 16 Measured negative value of the normalized velocity autocorrelation function, $-C(\tau)/\langle v^2\rangle$, as a function of delay time τ for six different samples (color coded). The two black dashed lines indicate the range of the fitted values of the exponent ε from $\varepsilon = -1.25$ (lower dashed line) to $\varepsilon = -1.46$ (upper dashed line).

$d_f = d = 2$. Indeed, we find from Fig. 11 that all of the measured MSD curves become linear in τ (diffusive) when $\langle \Delta \mathbf{r}^2(\tau)\rangle \gtrsim \ell_c^2$.

A standard method of finding the value of the exponent γ in eqn (22) is through the local slope of the log–log plot of the measured MDS curve.[51,52] This method, however, is not accurate if the measured $\langle \Delta \mathbf{r}^2(\tau)\rangle$ is not a pure power law and contains either a constant term or a linear term in τ.[14,51] To clarify this issue, we calculate the velocity autocorrelation function from the measured particle trajectories,

$$C(\tau) = \langle \mathbf{v}(t)\mathbf{v}(t+\tau)\rangle, \tag{26}$$

where $\mathbf{v}(t) = \Delta \mathbf{r}(t)/\Delta t$ is the instantaneous velocity with Δt being the shortest sampling time. Because the particles often encounter the same obstacle in the random field, their $C(\tau)$ is anti-correlated and thus is a negative quantity.[53] For a stationary system, one has[54]

$$C(\tau) = \frac{1}{2}\frac{d^2}{d\tau^2}\langle \Delta \mathbf{r}^2(\tau)\rangle. \tag{27}$$

We have verified this equation by a direct comparison between the calculated $C(\tau)$ and the second derivative of the measured $\langle \Delta \mathbf{r}^2(\tau)\rangle$. Taking the second derivative of the measured $\langle \Delta \mathbf{r}^2(\tau)\rangle$ can effectively eliminate contributions from a constant background or normal diffusion and thus can determine the value of γ more accurately.[14,51]

Fig. 16 shows the measured negative value of the normalized velocity autocorrelation function, $-C(\tau)/\langle v^2\rangle$, as a function of delay time τ in the log–log scale for six different samples. For large values of τ, the data have relatively larger uncertainties as the absolute value of $-C(\tau)/\langle v^2\rangle$ is very small. In this case, a moving average is taken to smooth out the high frequency noise. The measured $-C(\tau)$ in the crossover region, $1\ \mathrm{s} \lesssim \tau \lesssim 100\ \mathrm{s}$, for each sample is well described by the power law,

$$-C(\tau) \sim \tau^{\varepsilon}, \tag{28}$$

with the exponent ε varied in the range between -1.25 and -1.46 (two black dashed lines) for different samples. It is found that the fitted absolute value of ε increases slightly with the mean barrier height $\langle E_b\rangle$, and the average value of ε over all the samples is $\varepsilon = -1.35 \pm 0.11$.

From eqn (27) and (28), we find the exponent γ in eqn (22) can be written as $\gamma = 2 + \varepsilon$. With the measured mean value of ε, we find that $\gamma = 0.65 \pm 0.11$. This value of γ agrees well with the predicted value $\gamma = 0.695$ based on the percolation theory.[48] For the random potentials used in this experiment, there are additional energy barriers in the accessible void space. These energy barriers will affect the value of γ, as they can further hinder the colloidal diffusion. Because the mean barrier height $\langle E_b\rangle$ varies among different samples, the resulting value of γ is found to decrease slightly with the mean barrier height $\langle E_b\rangle$. Our measurement of the exponents d_f and γ thus confirms that colloidal diffusion over the 2D random potential can be adequately described by the Lorentz model.

It is also found that the values of γ obtained from Fig. 16 are all smaller than those obtained directly from the local slope of the measured MSD curves. For sample S6, the two values of γ differ by 0.19. For other samples, the difference is even bigger. This finding suggests that there is a significant contribution of normal diffusion to the measured $\langle \Delta \mathbf{r}^2(\tau)\rangle$ in the subdiffusion regime. For diffusion over a random potential, particles in different locations may take a different amount of time to reach their final long-time diffusion regime. The measured $\langle \Delta \mathbf{r}^2(\tau)\rangle$ in the subdiffusion regime is thus averaged over a heterogenous ensemble of particle trajectories with both diffusive and subdiffusive characteristics. By taking the second derivative of $\langle \Delta \mathbf{r}^2(\tau)\rangle$, the diffusive component (linear in τ) in the measured $\langle \Delta \mathbf{r}^2(\tau)\rangle$ is eliminated. We therefore conclude that the values of γ obtained from Fig. 16 are more accurate. A future study of non-power-law contributions to the measured $\langle \Delta \mathbf{r}^2(\tau)\rangle$ in the subdiffusion regime is needed for colloidal diffusion over complex potential landscapes.

V. Conclusion

In this work, we used a two-layer colloidal system to study colloidal diffusion over a quenched random potential. The bottom layer is made of a mixture of bidisperse silica spheres, which form a randomly packed colloidal monolayer on a glass substrate. The top layer consists of monodisperse silica spheres diffusing over the ragged surface of the bottom colloidal layer, which provides a random gravitational potential $U(x,y)$ to the diffusing particles in the top layer. By measuring the population probability histogram $P(x,y)$ of the top diffusing particles, we obtain $U(x,y)$ *via* the Boltzmann distribution in eqn (18). With the obtained $U(x,y)$, we find that the random potential for a fixed configuration of bottom layer particles is well described by a universal distribution function $H(E_b/\langle E_b\rangle)$ of the energy barrier height E_b, where the mean value $\langle E_b\rangle$ increases with the size of the top layer particles (see Table 1).

The dynamical properties of the top diffusing particles, such as their mean square displacement (MSD) $\langle \Delta \mathbf{r}^2(\tau) \rangle$, histogram $P(t_E)$ of the escape time t_E, and long-time self-diffusion coefficient D_L, are simultaneously measured from the particle trajectories. The measured MSD exhibits a dual-crossover behavior with an initial short-time diffusion followed by a crossover to the subdiffuion regime caused by the structural disorders in the bottom colloidal layer. When the delay time τ becomes more than five times longer than the largest mean escape time $(\bar{t}_E)_{max}$, the particles on average have experienced (or hopped over) many potential barriers, and their motion recovered back to normal diffusion with a reduced long-time diffusion coefficient D_L. The measured D_L is well described by eqn (17), which is obtained using the approach of potential path average as originally proposed by Zwanzig.[16]

The random field has two major effects on colloidal diffusion. First, it reduces the value of D_L. As the distribution of the barrier heights E_b is broad, larger values of E_b are found to play a more dominant role in suppressing the value of D_L. Second, the random field enlarges the subdiffusion region and delays the crossover time from subdiffusion to normal diffusion. Such a crossover can be explained by the Lorentz model for tracer diffusion through a heterogeneous space with a finite cutoff length ℓ_c. It is found that the area occupied by the particle trajectories (''path area'') in the random potential field is a fractal with fractal dimension $d_f = 1.83 \pm 0.02$, when the length scale ℓ is in the range $\ell_0 (\simeq 1\ \mu m) \lesssim \ell \lesssim \ell_c (\simeq 7\ \mu m)$. This value of d_f is very close to the predicted value $d_f = 91/48$ by the Lorentz model. When the particles diffuse in a fractal area, their motion is slowed down with increasing delay time τ and the resulting $\langle \Delta \mathbf{r}^2(\tau) \rangle$ becomes subdiffusive with the exponent $\gamma = 0.65 \pm 0.11$. This value of γ is in good agreement with the predicted value $\gamma = 0.695$ based on the percolation theory.[48] For larger length scales with $\ell > \ell_c$ (or longer delay times), the path area becomes homogeneous and the measured $\langle \Delta \mathbf{r}^2(\tau) \rangle$ is changed from subdiffusion to normal diffusion.

Our work demonstrates that the two-layer colloidal system is a versatile platform for the study of colloidal diffusion over complex potential landscapes. By using a mixture of bidisperse spheres with different particle sizes and number ratios, one can generate a randomly packed colloidal monolayer on the bottom with a large number of disorder configurations, which have a short correlation length comparable to the size of the top layer diffusing particles. The disorder configurations vary from crystal-like structures with different amounts of defects and grain boundaries introduced by the ''dopant'' particles to various glass-like structures with either well-mixed (homogenous) states or micro-structured domains.[39–41] It is even possible to use a mixture of polydisperse spheres with size ratios following a power law. This method thus provides a well-controlled and convenient way to vary the potential landscapes with different disorders. With the capability of simultaneous multi-particle tracking of the top-layer diffusing particles and determination of the underlying potential landscape at the single-particle spatial resolution, one is able to conduct quantitative studies of a range of interesting issues involved in colloidal diffusion over 2D random potentials, such as finding the correlations between the bottom-layer structures and energy barrier height distribution $H(E_b)$ as shown in Fig. 9, as well as dynamic heterogeneity of the top-layer diffusing particles. Clearly, the two-layer colloidal system is a rich system with a large parameter space to explore. The present work represents the first step towards this direction.

Acknowledgements

The authors wish to thank Bruce J. Ackerson for useful discussions. This work was supported in part by RGC of Hong Kong SAR under grant no. A-HKUST616/14-A (P. T.) and HKUST16302816 (P. T.), and by MoST of Taiwan under the grant no. 103-2112-M-008-003-MY3, (P. Y. L.).

References

1 J. W. Haus and K. W. Kehr, *Phys. Rep.*, 1987, **150**, 263.
2 J. P. Bouchaud and A. Georges, *Phys. Rep.*, 1990, **195**, 127.
3 S. Havlin and D. Ben-Avraham, *Adv. Phys.*, 2002, **51**(1), 187 (originally published in *Adv. Phys.*, 1987, **36**).
4 S. J. Harris, A. Timmons, D. R. Baker and C. Monroe, *Chem. Phys. Lett.*, 2010, **485**, 265–274.
5 L. Sieminskas, M. Ferguson, T. W. Zerda and E. Couch, *J. Sol-Gel Sci. Technol.*, 1997, **8**, 1105–1109.
6 G. Dagan, *J. Fluid Mech.*, 1984, **145**, 151.
7 F. Höfling and T. Franosch, *Rep. Prog. Phys.*, 2013, **76**, 046602.
8 Y. Meroz and I. M. Sokolov, *Phys. Rep.*, 2015, **573**, 1–29.
9 Y. Kafri, D. K. Lubensky and D. R. Nelson, *Biophys. J.*, 2004, **86**, 3373.
10 P. Smith, I. E. G. Morrison, K. M. Wilson, N. Fernandez and R. J. Cherry, *Biophys. J.*, 1999, **76**, 3331.
11 I. Golding and E. C. Cox, *Phys. Rev. Lett.*, 2006, **96**, 098102.
12 E. Barkai, Y. Garini and R. Metzler, *Phys. Today*, 2012, **65**(8), 29.
13 A. Kusumi, Y. Umemura, N. Morone and T. Fujiwara, in *Anomalous Transport: Foundations and Applications*, ed. R. Klages, G. Radons and I. M. Sokolov, Wiley-VCH Verlag GmbH & Co. KGaA, Weinheim, Germany, 2008, ch. 19, pp. 545–574.
14 W. He, H. Song, Y. Su, L. Geng, B. J. Ackerson, H. B. Peng and P. Tong, *Nat. Commun.*, 2016, **7**, 11701.
15 J. Bernasconi, H. U. Beyeler, S. Strassler and S. Alexander, *Phys. Rev. Lett.*, 1979, **42**, 819.
16 R. Zwanzig, *Proc. Natl. Acad. Sci. U. S. A.*, 1988, **85**, 2029.
17 D. S. Novikov, E. Fieremans, J. H. Jensen and J. A. Helpern, *Nat. Phys.*, 2011, **7**, 508.
18 P. J. H. Denteneer and M. H. Ernst, *Phys. Rev.*, 1984, **B29**, 1755.
19 K. W. Kehr, D. Richter and R. H. Swendsen, *J. Phys.*, 1978, **F8**, 433.
20 J. W. Haus, K. W. Kehr and J. W. Lyklema, *Phys. Rev. B: Condens. Matter Mater. Phys.*, 1982, **25**, 2905.
21 S. Lifson and J. L. Jackson, *J. Chem. Phys.*, 1962, **36**, 2410.

22 H. Scher and M. Lax, *Phys. Rev. B: Solid State*, 1973, **7**, 4491.
23 A. Lubelski, I. M. Sokolov and J. Klafter, *Phys. Rev. Lett.*, 2008, **100**, 250602.
24 R. Metzler and J. Klafter, *Phys. Rep.*, 2000, **339**, 1.
25 M. Evstigneev, O. Zvyagolskaya, S. Bleil, R. Eichhorn, C. Bechinger and P. Reimann, *Phys. Rev. E: Stat., Nonlinear, Soft Matter Phys.*, 2008, **77**, 041107.
26 R. D. L. Hanes, C. Dalle-Ferrier, M. Schmiedeberg, M. C. Jenkinsa and S. U. Egelhaaf, *Soft Matter*, 2010, **8**, 2714.
27 F. Evers, C. Zunke, R. D. L. Hanes, J. Bewerunge, I. Ladadwa, A. Heuer and S. U. Egelhaaf, *Phys. Rev. E: Stat., Nonlinear, Soft Matter Phys.*, 2013, **88**, 022125.
28 J. Bewerunge, I. Ladadwa, F. Platten, C. Zunke, A. Heuer and S. U. Egelhaaf, *Phys. Chem. Chem. Phys.*, 2016, **18**, 18887.
29 X. G. Ma, P. Y. Lai and P. Tong, *Soft Matter*, 2013, **9**, 8826.
30 Y. Roichman, B. Sun, Y. Roichman, J. Amato-Grill and D. G. Grier, *Phys. Rev. Lett.*, 2008, **100**, 013602.
31 B. Sun, J. Lin, E. Darby, A. Y. Grosberg and D. G. Grier, *Phys. Rev. E: Stat., Nonlinear, Soft Matter Phys.*, 2009, **80**, 010401(R).
32 X. G. Ma, P. Y. Lai, B. J. Ackerson and P. Tong, *Soft Matter*, 2015, **11**, 1182.
33 X. G. Ma, W. Chen, Z.-R. Wang, Y. Peng, Y.-L. Han and P. Tong, *Phys. Rev. Lett.*, 2013, **110**, 078302.
34 P. Hanggi, P. Talkner and M. Borkovec, *Rev. Mod. Phys.*, 1990, **62**, 251.
35 S. Arrhenius, *Z. Phys. Chem.*, 1889, **4**, 226.
36 H. A. Kramers, *Physica*, 1940, **7**, 284.
37 J. V. Barth, H. Brune, B. Fischer, J. Weckesser and K. Kern, *Phys. Rev. Lett.*, 2000, **84**, 1732.
38 G. L. Hunter and E. R. Weeks, *Phys. Rev. E: Stat., Nonlinear, Soft Matter Phys.*, 2012, **85**, 031504.
39 A. Imhof and J. K. G. Dhont, *Phys. Rev. Lett.*, 1995, **75**, 1662.
40 P. Yunker, Z.-X. Zhang and A. G. Yodh, *Phys. Rev. Lett.*, 2010, **104**, 015701.
41 N. Xu and E. S. C. Ching, *Soft Matter*, 2010, **6**, 2944.
42 J. C. Crocker and D. G. Grier, *J. Colloid Interface Sci.*, 1996, **179**, 298.
43 A. Ghosh, V. Chikkadi, P. Schall and D. Bonn, *Phys. Rev. Lett.*, 2011, **107**, 188303.
44 G. L. Hunter and E. R. Weeks, *Rep. Prog. Phys.*, 2012, **75**, 066501.
45 H. A. Lorentz, *Arch. Neerl. Sci. Exactes Nat.*, 1905, **10**, 336.
46 B. O'Shaughnessy and I. Procaccia, *Phys. Rev. A: At., Mol., Opt. Phys.*, 1985, **32**, 3073.
47 A. Kammerer, F. Höfling and T. Franosch, *Europhys. Lett.*, 2008, **84**, 66002.
48 P. Grassberger, *Physica A*, 1999, **262**, 251.
49 T. Bauer, F. Höfling, T. Munk, E. Frey and T. Franosch, *Eur. Phys. J.: Spec. Top.*, 2010, **189**, 103.
50 S. Havlin and A. Bunde, *Fractals and disordered systems*, Springer, London, 1991.
51 D. S. Martin, M. B. Forstner and J. A. Käs, *Biophys. J.*, 2002, **83**, 2109.
52 I. Y. Wong, M. L. Gardel, D. R. Reichman, E. R. Weeks, M. T. Valentine, A. R. Bausch and D. A. Weitz, *Phys. Rev. Lett.*, 2004, **92**, 178101.
53 T. Franosch, F. Höfling, T. Bauer and E. Frey, *Chem. Phys.*, 2010, **375**, 540.
54 D. Jacobs and H. Nakanishi, *Phys. Rev. A: At., Mol., Opt. Phys.*, 1990, **41**, 706.